Acta Crystallographica Section D
Biological Crystallography
ISSN 0907-4449

Changes to crystals of *Escherichia coli* β-galactosidase during room-temperature/low-temperature cycling and their relation to cryo-annealing

Douglas H. Juers,[a,b]* Jeffrey Lovelace,[c] Henry D. Bellamy,[d] Edward H. Snell,[e] Brian W. Matthews[a] and Gloria E. O. Borgstahl[c]

[a]Howard Hughes Medical Institute, Institute of Molecular Biology and Department of Physics, 1229 University of Oregon, Eugene, OR 97405, USA, [b]Department of Physics, Whitman College, Walla Walla, WA 99362, USA, [c]Eppley Institute for Research in Cancer and Allied Diseases, 987696 Nebraska Medical Center, Omaha, NE 68198-7696, USA, [d]Center for Advanced Microstructures and Devices, Louisiana State University, 6980 Jefferson Highway, Baton Rouge, LA 70806, USA, and [e]Hauptman–Woodward Medical Research Institute and SUNY Buffalo Department of Structural Biology, 700 Ellicot Street, Buffalo, NY 14203, USA

Correspondence e-mail: juersdh@whitman.edu

Received 7 June 2007
Accepted 14 September 2007

Flash-cooling of macromolecular crystals often compromises diffraction quality by increasing the mosaicity. In some cases, cycling the crystal between low temperature (LT) and room temperature (RT) can reverse this increase in mosaicity. Previous studies of RT/LT cycling have focused on the quality of the crystal as it was repeatedly returned to the LT state. Here, crystal quality is explored not only at LT but also when the crystal is returned to RT. The domain model is used to extract information about crystal order from reflection profiles measured from crystals of *Escherichia coli* β-galactosidase at both temperatures. Despite optimization of the cryocooling protocol, the mosaicity increases by about sixfold with cooling and is anisotropic at both temperatures. The mosaicity increase is the consequence of a decrease in domain volume, an increase in the variation of domain cell dimensions and an increase in the angular spread between domains. Upon rewarming, the mosaicity recovers substantially, including the somewhat surprising recovery of domain volume, but incompletely. Over multiple RT/LT cycles disorder in both states increases, which appears to mainly arise from radiation damage, although a contribution from cool–thaw processes cannot be ruled out. The analysis further suggests that LT disorder is governed by variability inherent in the cooling process combined with the overall history of the crystal. In contrast, RT disorder appears to be governed principally by the overall history of the crystal. This suggests that with these particular crystals under the experimental conditions used, particularly at high-intensity synchrotron X-ray sources, RT/LT cycling annealing protocols should involve few cycles so as to limit the hysteresis in both temperature states while taking advantage of the inherent variability in the cooling process that may result in improved crystal order at LT.

1. Introduction

Macromolecular crystals are commonly cooled to low temperature (LT) for X-ray data collection as a way of mitigating damage arising from the ionizing radiation (Hope, 1988; Rodgers, 1994; Garman & Schneider, 1997; Garman, 1999; Garman & Doublié, 2003; Hanson *et al.*, 2003). Typically, a crystal is rapidly cooled ('flash-cooled') and maintained at ∼100 K with a nitrogen-gas stream. With some crystals, such cooling is absolutely required to record high-resolution diffraction data. Flash-cooling is now so predominant in macromolecular crystallography, especially at high-intensity synchrotron-radiation sources, that robots have been developed to rapidly screen hundreds of crystals stored in liquid-nitrogen Dewars. Room-temperature (RT) data collection at synchrotrons has become the exception rather than the rule (Garman & Owen, 2006).

Although data collection at LT diminishes radiation-induced crystal damage, the cooling process itself can be deleterious to crystal order. The severity of this cooling-induced damage ranges from a small increase in spot width to the complete disappearance of discernable diffraction spots. However, in some cases crystal order lost from cooling-induced damage can be recovered. The recovery process, called crystal annealing or crystal healing, involves cycling the crystal between LT and some higher temperature (usually RT).

Many successful applications of annealing have been reported. Some examples include the nucleosome core particle, in which RT/LT cycling decreased the mosaicity by more than twofold (Harp *et al.*, 1998); the histone octamer, in which the mosaicity decreased by 20% (Harp *et al.*, 1998); glycerol kinase, in which multiple RT/LT cycles improved the resolution limit from 3.6 to 2.8 Å and the mosaicity decreased twofold (Yeh & Hol, 1998); and nitrite reductase, in which the resolution improved from 2.5 to 1.0 Å (Ellis *et al.*, 2002).

The physical basis of annealing is under investigation (Harp *et al.*, 1999; Kriminski *et al.*, 2002; Parkin & Hope, 2003; Juers & Matthews, 2004; Weik *et al.*, 2005). In some cases, it appears to be related to whether the cryoprotectant is at its optimal concentration (Mitchell & Garman, 1994), involving transport of water into or out of the crystal during the warming phase, effectively adjusting the cryoprotectant concentration towards a more optimal value (Juers & Matthews, 2004). In the system used for this study, the optimal cryoprotectant concentration is about 30%(*v*/*v*) dimethyl sulfoxide (DMSO). Here, annealing *via* RT/LT cycling appears to be most effective (that is, produces the most dramatic improvement in diffraction quality) when the crystals are initially somewhat above this optimal cryoprotectant concentration.

In all the cases described above, diffraction measurements were only made at LT. It is therefore unknown to what extent the crystals recover during the warming phase before recooling. A key question for understanding annealing mechanisms is whether damage from cooling can be completely reversed with warming. If the crystal completely recovers with warming, whatever the order at LT, the implications for annealing are that the number of annealing cycles is irrelevant and cool–thaw cycling can in principle be carried out with impunity until the best diffraction is found. On the other hand, if there were a build-up of crystal damage with successive cycles then only a limited number of annealing cycles would be possible.

Here, we present the results of experiments designed to address these questions. We recorded reflection profiles from crystals cycled repeatedly between RT (∼295 K) and LT (∼100 K), making measurements on the same crystal at both temperatures in order to directly measure the reversibility of cooling. In the system studied, cooling-induced lattice damage was largely recoverable, with some hysteresis.

We used the orthorhombic crystal form of *Escherichia coli* β-galactosidase, a well characterized system for cryocooling experiments. The crystals belong to space group $P2_12_12_1$, with unit-cell parameters a = 154, b = 174, c = 204 Å at RT. The asymmetric unit consists of one β-galactosidase homotetramer (MW = 460 kDa) and about 57% of the crystal volume is occupied by bulk solvent. In this system, penetrating cryoprotectants such as DMSO or polyethylene glycol (PEG) 400 are required to successfully flash-cool the crystals. This cooling causes the mosaicity to increase, the unit cell to shrink by 5% in volume and the lattice to repack in such a way that the surface area buried at crystal contacts increases by approximately 50%. Initial experiments suggested that these changes were reversible for up to five cycles of cooling and warming (Juers & Matthews, 2001). Here, we analyze this phenomenon in more detail, focusing on the changes in mosaicity.

With typical X-ray beams designed for high-resolution structural data collection, mosaicity measurements are dominated by the geometric and spectral contributions of the beam rather than the true mosaicity of the crystal (Greenhough & Helliwell, 1982*a*). The crystal mosaicity can be probed by minimizing the X-ray beam divergence and deconvoluting beam effects. Here, we used a nearly parallel and monochromatic X-ray beam in combination with a 'fine φ-slicing method' (Bellamy *et al.*, 2000) to accurately determine profiles for a statistically significant number of reflections, yielding a description of the progression of disorder in β-galactosidase crystals as they are cycled repeatedly between RT and LT.

2. Materials and methods

2.1. Crystals

Unless noted otherwise, all chemicals were purchased from Sigma (St Louis, MO, USA). Crystals of *E. coli* β-galactosidase in the orthorhombic crystal form were prepared as reported previously (Juers *et al.*, 2000). They were harvested into a mother liquor consisting of 100 m*M* bis-Tris pH 6.5, 200 m*M* $MgCl_2$, 100 m*M* NaCl, 10 m*M* dithiothreitol (DTT) (BioVectra DCL, Oxford, CT, USA) and 10%(*w*/*v*) PEG 8000 (Hampton Research, Aliso Viejo, CA, USA) and stored at RT. Two crystals were examined under these conditions. Otherwise, all crystals were slowly equilibrated to a cryosolution consisting of 70%(*v*/*v*) mother liquor and 30%(*v*/*v*) DMSO (Juers *et al.*, 2000) prior to X-ray analysis (either at RT or LT).

The cryosolution equilibration was achieved by initially pipetting a few crystals into one side of a small flat-bottomed rubber-stoppered glass vial (about 1.5 cm in diameter and 1.5 cm tall) containing 700 µl mother liquor. To equilibrate the crystals, a small amount of cryoprotectant was pipetted into the mother liquor directly opposite the crystals on the other side of the vial, mixed *via* pipetting and allowed to diffuse into the region containing the crystals. This was performed with 25 µl (for the first few additions) or 50 µl (for the last few additions) aliquots at approximately 1 h time intervals until a total of 300 µl cryoprotectant had been added, giving a total equilibration time of several hours. After this process, the crystals were transferred to a fresh 1 ml vial of cryosolution that had been mixed using a larger (50 ml) volume in order to minimize the uncertainties associated with pipetting.

The optimal cryoprotectant concentration had been determined previously by equilibrating crystals to a range of

Table 1
Summary of crystal and data-collection parameters.

	Crystal descriptors			Unit-cell parameters							
Type†	Crystal	Condition‡	Size (100 µm)§	*a* (Å)	*b* (Å)	*c* (Å)	Volume (Å^3 × 10^{-6})	Total reflections¶	d_{avg}†† (Å)	d_{min}†† (Å)	I_{avg}‡‡
I	9	RT-1	3/3/3	153.9	171.9	204.9	5.42	4371	5.0	3.2	401
	17	RT-1	—	153.9	171.7	204.9	5.41	5035	5.1	3.2	406
II	18	RT-1	—	153.3	171.2	204.1	5.36	2956	5.6	3.2	201
	2	RT-1	2/4/4	153.2	170.9	204.0	5.34	3086	5.3	3.2	197
		LT-1		149.5	168.1	200.8	5.05	339	8.7	3.8	89
		RT-2		153.6	171.2	204.3	5.37	1250	6.4	3.4	142
	10	RT-1	4/5/6	153.5	171.0	204.1	5.36	4331	5.1	3.2	302
		LT-1		149.9	168.4	201.1	5.08	5087	5.3	3.2	155
		RT-2		153.3	171.1	204.2	5.36	3056	5.4	3.2	141
	3	RT-1	3/4/5	153.5	171.0	204.2	5.36	2937	5.4	3.2	203
		LT-1		149.6	168.0	200.7	5.05	925	6.8	3.5	97
		RT-2		153.4	171.1	204.1	5.36	2723	5.4	3.2	184
		LT-2		149.9	167.3	200.7	5.04	694	7.6	3.4	100
		RT-3		153.5	171.1	204.2	5.36	1038	6.4	3.3	120
	16	RT-1	2/3/4	153.5	171.1	204.2	5.36	5458	4.9	3.2	535
		LT-1		150.4	167.5	201.1	5.07	2156	6.0	3.3	116
		RT-2		153.6	171.3	204.4	5.38	2889	5.4	3.2	202
		LT-2		151.1	166.9	201.3	5.08	1606	7.1	3.3	141
		RT-3		153.4	171.0	204.4	5.36	2112	5.8	3.2	179
	8	RT-1	2/5/5	153.5	171.1	204.2	5.36	5477	4.9	3.2	618
		LT-1		150.3	168.4	201.1	5.10	4495	5.2	3.2	156
		RT-2		153.4	171.2	204.1	5.36	3103	5.5	3.2	239
		LT-2		151.3	167.7	201.2	5.11	1398	7.1	3.5	127
		RT-3		153.3	171.1	204.2	5.36	2044	5.8	3.2	179
		LT-3		151.6	167.2	201.1	5.10	1470	6.7	3.3	103
		RT-4		153.4	171.0	204.0	5.35	1002	6.2	3.2	111
IIIa	5	LT-1	4/4/5	149.5	167.0	200.5	5.01	2332	5.8	3.2	116
	15	LT-1	3/6/6	149.7	168.4	200.8	5.06	8815	4.9	3.2	248
	4	LT-1	2/3/3	149.5	167.8	200.3	5.02	6247	5.1	3.2	191
		LT-2		149.5	167.6	200.5	5.02	3005	5.6	3.2	122
		LT-3		149.6	167.2	200.5	5.02	4665	5.2	3.2	147
		LT-4		150.1	166.3	200.4	5.00	410	8.7	3.2	116
		LT-5		150.8	167.2	201.2	5.07	528	8.0	3.2	106
	6	LT-1	5/5/5	149.5	167.0	200.1	4.99	4602	5.3	3.2	151
		LT-2		149.5	167.6	200.2	5.02	1470	6.1	3.2	108
		LT-3		149.6	167.7	200.4	5.03	914	7.2	3.5	94
		LT-4		150.3	167.8	201.0	5.07	659	7.5	3.8	78
IIIb	11	LT-2	5/6/7	149.6	168.5	200.9	5.06	7603	4.9	3.2	218
		LT-3		149.7	168.2	200.8	5.06	5221	5.1	3.2	170
	13	LT-2	4/4/4	149.6	168.7	200.7	5.07	8163	4.9	3.2	233
	14	LT-2	4/4/4	149.5	168.2	200.6	5.04	6263	4.9	3.2	176
Controls§§											
	7	LT-1	2/3/4	149.5	167.6	200.4	5.02	8196	5.1	3.2	187
		LT-2		149.4	167.6	200.4	5.02	9383	5.0	3.2	209
		LT-3		149.5	167.6	200.4	5.02	8991	5.0	3.2	199
	12	LT-1	6/7/7	149.5	168.0	200.2	5.03	2107	5.9	3.2	108
		RT-2		153.8	171.0	204.6	5.38	132	8.9	3.2	103

† Three types of experiments were performed (see text). ‡ RT and LT refer to room temperature and low temperature, respectively. The number refers to the cycle number (*e.g.* LT-2 indicates the second time the crystal was at LT during RT/LT cycling). § Length of each crystal dimension in 100 µm units. The crystal size was not recorded for crystals 17 and 18. ¶ Total number of reflections analyzed after rejection of poor profiles. Rejection criteria are given in the text. †† d_{avg} is the average and d_{min} is the highest resolution of the reflections analyzed. ‡‡ I_{avg} is the average maximum peak intensity in arbitrary units §§ Crystal 7 was exposed repeatedly at LT without a warming phase as a control for radiation damage at LT. Crystal 12 was not exposed in the initial room-temperature phase as a control for radiation damage at room temperature.

cryoprotectant concentrations in 5% increments. About 30%(*v*/*v*) DMSO was judged to be optimal based on inspection of images (spots were the tightest and diffuse scatter was minimal) and minimum mosaicity estimations using *MOSFLM* (Leslie, 1992).

2.2. Room-temperature/low-temperature (RT/LT) cycling

For RT data collection a capillary mount was used rather than a loop mount in order to use easily reproducible humidity conditions. Each crystal to be measured at RT was mounted in the glass capillary using either the mother liquor or the cryosolution described above. A small plug of this mounting solution was left on either side of the crystal to prevent it from drying out and the capillary was sealed with wax. For crystals to be cycled between RT and LT, the wax was removed after RT measurements were recorded and the crystal was expelled from the capillary into an ∼300 µl drop of the cryosolution. The crystal was then scooped up into a cryoloop (Hampton Research) and flash-cooled by blocking the cryostream with a microscope slide, placing the loop on the goniometer and unblocking the cryostream. After data at LT had been

collected, the crystal was removed from the cryostream and incubated in an ∼300 µl drop of the cryosolution for about 3 min before remounting in a capillary. These conditions were used in order to be consistent with the annealing experiments previously reported by Harp *et al.* (1999).

Three types of experiments were performed (see Table 1). In type I experiments, data were collected from two crystals at RT with no cryoprotectant. These crystals experienced minimal handling and provided a baseline control. In type II experiments, data were collected from cryoprotected crystals [30%(*v*/*v*) DMSO], cycling between RT and LT. In type III experiments, data were only collected at LT, with cryoprotected crystals cycling between RT and LT. In type IIIa experiments data were collected after each cooling cycle, while in type IIIb experiments data were collected starting after the second cooling cycle. The type III experiments were intended to serve as controls for radiation-damage effects.

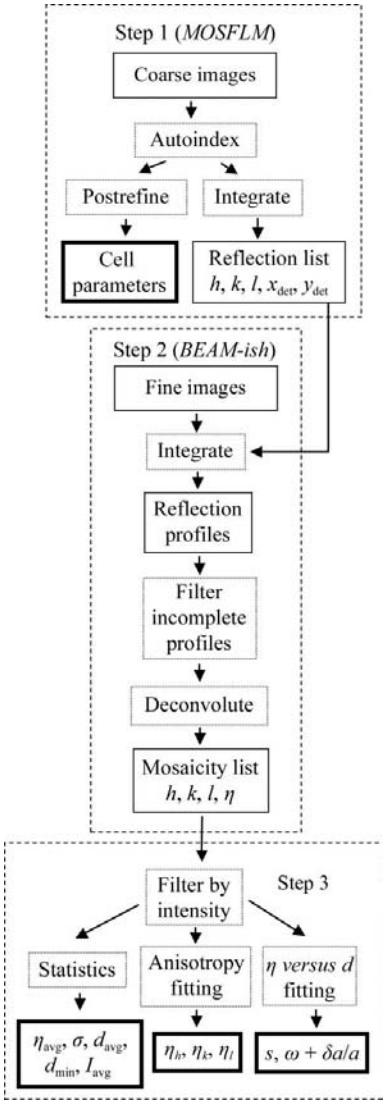

Figure 1
Flow diagram showing the steps in data processing and analysis for each crystal at each temperature. The small solid boxes refer to data sets, which are then analyzed by the actions in the small dotted boxes. Actions in step 1 were performed with *MOSFLM* (Leslie, 1992), those in step 2 with *BEAM-ish* (Lovelace & Borgstahl, 2003) and those in step 3 with *Igor Pro* (Wavemetrics, Lake Oswego, Oregon, USA), as well as other programs written by the authors. For details see §2. The four boxes with bold edges correspond to the final results and are listed in Tables 1 and 2.

2.3. Fine φ-sliced data collection

The Advanced Photon Source (APS) beamline ID17, which is administered by the Industrial Macromolecular Crystallography Association Collaborative Access Team (IMCA-CAT), was used in unfocused mode to minimize beam divergence (Bellamy *et al.*, 2000). The beam properties were calculated from the source size with the 0.1 mm beam-defining square aperture 63.0 m from the source. For collection of data sets the horizontal and vertical beam divergences were 16 and 6 µrad, respectively, and the beam bandwidth, $\delta\lambda/\lambda$, was 4.00×10^{-4}. The double-crystal monochromator used should cause no significant change in energy across the 0.1 mm beam (*i.e.* negligible correlated dispersion). In order to obtain a statistically significant number of measurements in a reasonable amount of beam time, data were collected with a Quantum-210 CCD detector (ADSC) using rotation-camera geometry as described previously (Bellamy *et al.*, 2000; Borgstahl *et al.*, 2001; Snell *et al.*, 2001). For all measurements the wavelength was 1.200 Å (10.30 keV) and the beam was collimated to 0.1 mm in each direction. For RT data, in order to determine the crystal orientation, two orthogonal 3° swaths of coarse data were collected ($\Delta\varphi$ = 0.5° with 0.5 s exposure) and processed with *MOSFLM* (Leslie, 1992). Fine φ-sliced data were then collected for mosaicity measurements from the first 1.25° of the coarse range ($\Delta\varphi$ = 0.005° with 0.5 s exposure). To reduce the amount of radiation damage to the crystal, 225 µm of Al was used to attenuate the beam by a factor of four during the fine data collection. For the cryogenic data, the same coarse data procedure was followed; however, the fine φ-sliced data were collected in 0.01° oscillations with 0.5 s exposures over the entire range of the coarse images. The beam was again attenuated fourfold for the fine data collection. Each set of coarse and fine measurements at either LT or RT took a total of about 5 min. The space group was $P2_12_12_1$, with typical unit-cell parameters a = 154, b = 174, c = 204 Å at RT and a = 150, b = 168, c = 201 Å at ∼100 K. The crystal-to-detector distance was 175 mm for all measurements. The data were collected in constant-time mode and were not corrected for the change in beam intensity with ring current. In general, the ring current decreased from 100 to 80 mA over a 12 h period between ring fills. Fills were accomplished with the fill-on-fill approach (no down time between fills) and no beam dumps occurred during data collection. Therefore, the change in beam intensity during the time a given reflection was being collected was negligible.

2.4. Data processing

The fine φ-sliced data were processed and the reflection profiles were analyzed using *BEAM-ish* 2.0 (Lovelace & Borgstahl, 2003; Lovelace *et al.*, 2000; see Fig. 1). For each swath of data, *BEAM-ish* uses *MOSFLM* to process the coarse

Table 2
Summary of crystal order parameters.

Type†	Crystal	Condition†	η (σ_η)‡ (mrad)	η_h§ (mrad)	η_k§ (mrad)	η_l§ (mrad)	R^2	m (σ_m)¶ (μrad Å^{-1})	s†† (μm)	$\omega + \delta a/a$‡‡ (mrad)
I	9	RT-1	0.7 (0.2)	0.7	1.0	0.8	0.96	0 (2)	>10.0	0.7
	17	RT-1	0.7 (0.2)	0.6	0.6	0.9	0.95	5 (1)	>10.0	0.7
II	18	RT-1	0.9 (0.4)	0.9	0.7	1.4	0.92	5 (3)	>10.0	0.9
	2	RT-1	0.6 (0.2)	0.6	0.7	0.8	0.91	2 (2)	>10.0	0.6
	2	LT-1	4.2 (1.6)	3.4	6.0	4.0	0.89	220 (18)	0.5	2.3
	2	RT-2	1.4 (0.4)	1.5	1.8	1.4	0.95	1 (6)	>10.0	1.4
	10	RT-1	0.7 (0.3)	0.9	0.9	0.6	0.90	10 (2)	9.6	0.7
	10	LT-1	5.0 (1.7)	6.2	5.2	4.9	0.90	240 (13)	0.4	3.8
	10	RT-2	1.1 (0.6)	1.0	1.3	1.4	0.80	31 (5)	3.2	0.9
	3	RT-1	0.7 (0.2)	0.8	0.9	0.8	0.97	7 (2)	>10.0	0.7
	3	LT-1	4.2 (2.0)	5.7	5.4	4.5	0.84	110 (23)	0.9	3.4
	3	RT-2	0.9 (0.4)	0.7	0.8	1.4	0.91	8 (3)	>10.0	0.8
	3	LT-2	3.5 (1.4)	4.3	5.3	3.4	0.92	17 (20)	6.1	3.4
	3	RT-3	1.7 (0.6)	3.0	1.4	1.1	0.92	59 (9)	1.7	1.3
	16	RT-1	0.7 (0.2)	0.7	0.7	0.8	0.92	3 (1)	>10.0	0.6
	16	LT-1	4.2 (2.2)	7.9	3.8	2.3	0.82	168 (16)	0.6	3.2
	16	RT-2	1.2 (0.5)	1.2	1.6	1.1	0.89	71 (6)	1.4	0.8
	16	LT-2	3.8 (1.2)	3.7	4.3	3.8	0.93	−14 (6)	−7.2	3.8
	16	RT-3	1.5 (0.7)	2.1	1.6	1.3	0.87	7 (5)	>10.0	1.5
	8	RT-1	0.8 (0.3)	0.8	0.8	0.9	0.92	10 (2)	9.8	0.7
	8	LT-1	4.7 (2.7)	11.7	3.6	2.1	0.85	317 (23)	0.3	3.0
	8	RT-2	1.4 (0.6)	2.0	1.1	1.7	0.92	48 (4)	2.1	1.2
	8	LT-2	5.7 (1.7)	7.4	5.5	5.7	0.94	103 (21)	1.0	5.0
	8	RT-3	1.6 (0.6)	1.8	1.4	1.9	0.91	37 (7)	2.7	1.4
	8	LT-3	5.8 (2.7)	4.4	7.3	7.1	0.82	207 (30)	0.5	4.5
	8	RT-4	1.4 (0.9)	0.7	2.3	1.5	0.82	58 (13)	1.7	1.0
IIIa	5	LT-1	2.8 (1.7)	2.3	3.0	4.8	0.79	136 (15)	0.7	2.0
	15	LT-1	2.6 (0.8)	2.8	3.8	1.6	0.98	11 (4)	8.8	2.5
	4	LT-1	2.5 (0.8)	2.4	3.7	2.1	0.93	73 (6)	1.4	2.1
	4	LT-2	3.9 (1.6)	4.1	4.6	3.9	0.89	0 (11)	>10.0	3.9
	4	LT-3	3.5 (1.1)	3.0	3.7	3.5	0.91	68 (10)	1.5	3.2
	4	LT-4	8.0 (2.3)	9.6	11.9	6.6	0.97	189 (30)	0.5	6.4
	4	LT-5	8.5 (2.2)	10.4	11.6	8.0	0.99	121 (22)	0.8	7.5
	6	LT-1	2.7 (0.8)	1.7	3.5	2.9	0.97	2 (4)	>10.0	2.7
	6	LT-2	5.0 (1.2)	4.8	5.0	5.5	0.96	132 (12)	0.8	4.2
	6	LT-3	8.3 (2.9)	7.2	14.7	7.5	0.95	216 (23)	0.5	6.9
	6	LT-4	5.5 (3.1)	8.1	9.2	4.8	0.86	260 (24)	0.4	3.5
IIIb	11	LT-2	2.9 (1.2)	2.0	4.4	2.8	0.91	65 (6)	1.5	2.5
	11	LT-3	2.7 (0.8)	2.3	2.7	2.9	0.93	94 (5)	1.1	2.2
	13	LT-2	2.7 (0.8)	2.3	2.6	3.2	0.98	36 (4)	2.8	2.5
	14	LT-2	3.1 (1.6)	6.5	1.7	3.0	0.88	134 (14)	0.7	2.4
Controls§§										
	7	LT-1	2.4 (0.6)	2.1	2.9	2.5	0.98	4 (3)	>10.0	2.4
	7	LT-2	2.4 (0.6)	2.1	2.9	2.5	0.98	−3 (3)	>10.0	2.5
	7	LT-3	2.5 (0.6)	2.1	2.9	2.5	0.98	2 (3)	>10.0	2.4
	12	LT-1	6.8 (2.9)	9.4	8.3	7.0	0.93	73 (21)	1.4	6.3
	12	RT-2	1.2 (0.5)	0.1	1.0	1.6	0.90	18 (12)	5.6	1.0

† See Table 1. ‡ η is the average mosaicity based on full-width at half-maximum (FWHM). The standard deviation of the population is in parentheses. § Anisotropy parameters. η_h, η_k, η_l indicate the mosaicity in each direction in reciprocal space. R^2 indicates the goodness of fit for the anisotropy fitting algorithm (see §2). ¶ Slope, m, of a linear fit of η to d, with the uncertainty in m from the linear fitting algorithm. †† Estimate of domain size s based on m ($s = 1/m$). ‡‡ Intercept of a linear fit of η to d ($= \omega + \delta a/a$; see §2). §§ See footnote in Table 1.

images and obtain the unit-cell parameters and crystal orientation matrix. The integration in *MOSFLM* was performed to 3.2 Å for most crystals in order to provide consistent resolution limits. A few crystals diffracted more weakly than typical, in which case the resolution limit was decreased to give about the same signal-to-noise in the highest resolution bin as for the other crystals [typically $I/\sigma(I) > 2.0$]. *MOSFLM* produces a list of all the theoretically observable reflections and their expected positions. These predicted positions are then used by *BEAM-ish* to integrate each spot (subtracting the background) on each of the fine-slice images for that swath. Intensity *versus* φ is then plotted to yield a profile of the reflection (Lovelace *et al.*, 2000). These profiles are processed to remove zingers (Borgstahl *et al.*, 2001) and then smoothed with a traveling window that averages the intensity. The window size was set such that the ratio of the filtering window to the reflection width was similar for RT and LT data (a window size of three images and five images was used for RT and LT data, respectively). In order to be accepted for profile analysis, the reflections had to have $I_{\max} > 50$. This cutoff was chosen as slightly above the minimum required to give a normal intensity distribution for all crystals. The mosaicity, η, was deconvoluted from the measured reflection full-width at half-maximum (FWHM), φ_R,

$$\eta = \frac{|\varphi_R| - (L^2\zeta^2\gamma_h^2 + \gamma_v^2)^{1/2}}{Ld^* \cos\theta_{hkl}} - \left(\frac{\delta\lambda}{\lambda}\right)\tan\theta_{hkl}. \quad (1)$$

Here, γ_v and γ_h are the vertical and horizontal crossfire angles at the sample, $\delta\lambda/\lambda$ is the beam bandwidth, L is the Lorentz correction, ζ is the position, in reciprocal-lattice units, of the corresponding reciprocal-lattice point projected onto the rotation axis and $d^* = \lambda/d$ (where d is the resolution; $d = \lambda/2\sin\theta_{hkl}$). It is assumed that there is no correlated dispersion. The derivation of this equation and the effects of these parameters on reflection broadening have been described previously (Bellamy *et al.*, 2000; Helliwell, 1992).

To calculate anisotropic mosaicity values for the crystals, the Ferrer and Roth model of anisotropic mosaicity was used (Fig. 1; Ferrer & Roth, 1998). The model is described by

$$\eta_{hkl}^{\rm calc} = \frac{\eta_h h^2 + \eta_k k^2 + \eta_l l^2}{h^2 + k^2 + l^2}. \quad (2)$$

Here h, k and l are the reflection indices and η_h, η_k and η_l represent the component of mosaicity along these directions, respectively. This model projects mosaicity components onto an ellipsoid. It is possible to solve the anisotropic components using a matrix-based form of multivariate regression. The multivariate analysis can sometimes result in nonphysical values (negative values) for η. In order to avoid this problem, a differential evolution algorithm was used to fit anisotropic mosaicities from the data (Wormington *et al.*, 1999). The differential evolution algorithm allows constrained fitting and has proven robust for other applications (Wormington *et al.*, 1999; Vahedi-Faridi *et al.*, 2003; Lovelace *et al.*, 2004, 2005, 2006). Once the anisotropic mosaicities had been calculated, the Pearson's coefficient of regression (R^2) was calulated in the standard fashion.

The data were harvested for all crystals using a script (*GNU Octave* v.2.1.50) that sequentially scanned all of the processed data and then limited the analysis to the reflection profiles that matched the acceptability filters for intensity and detector location. The script grouped results by crystal, cycle and swath. The results for each temperature cycle per crystal are shown in Table 2.

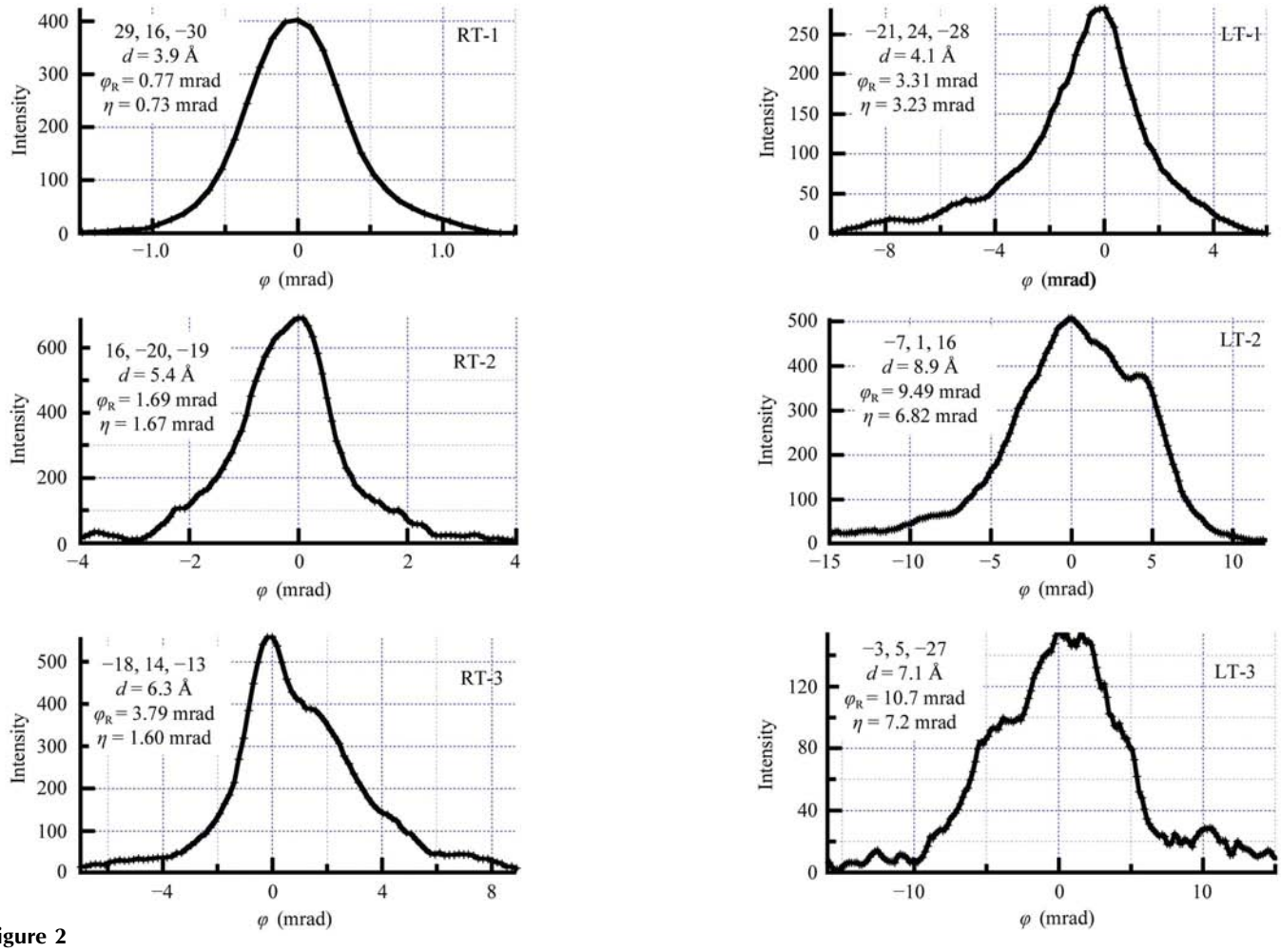

Figure 2
Reflection profiles showing integrated intensity *versus* oscillation angle. All profiles are from the same crystal (8) under successive cycles of RT and LT data collection. Because the crystal orientation was lost between cooling and thawing, it was not possible to follow the same reflection. The full-width at half-maximum of the shown profile was used as φ_R, which was then deconvoluted in a manner dependent on h, k, l and the beam parameters to yield η (1).

3. Results

Some examples of reflection profiles obtained using the fine φ-slicing technique are shown in Fig. 2. For each profile, we measured the FWHM and equated this to the reflecting range φ_R. The reflecting range depends on beam characteristics (crossfire and bandwidth), geometrical aspects of the rotation method (Lorentz factor) and imperfections in the crystal (mosaicity). The beam characteristics and Lorentz factor were removed from φ_R to give a value for the mosaicity, η, for each reflection (1). Fig. 3 shows plots of η *versus* d and η *versus* I for the LT-1 and RT-1 passes of crystal 10.

For the IMCA beam parameters, a perfect crystal with an infinite number of unit cells ($\eta = 0$) would have φ_R of the order of 10–100 µrad (depending on the diffraction angle and spot location, which determine the Lorentz factor and the amount of broadening arising from the finite incident-energy bandwidth). Because φ_R ranges from 0.5 mrad to a few milliradians, for most reflections φ_R is dominated by η (Fig. 2), which permits information about the crystal order to be determined.

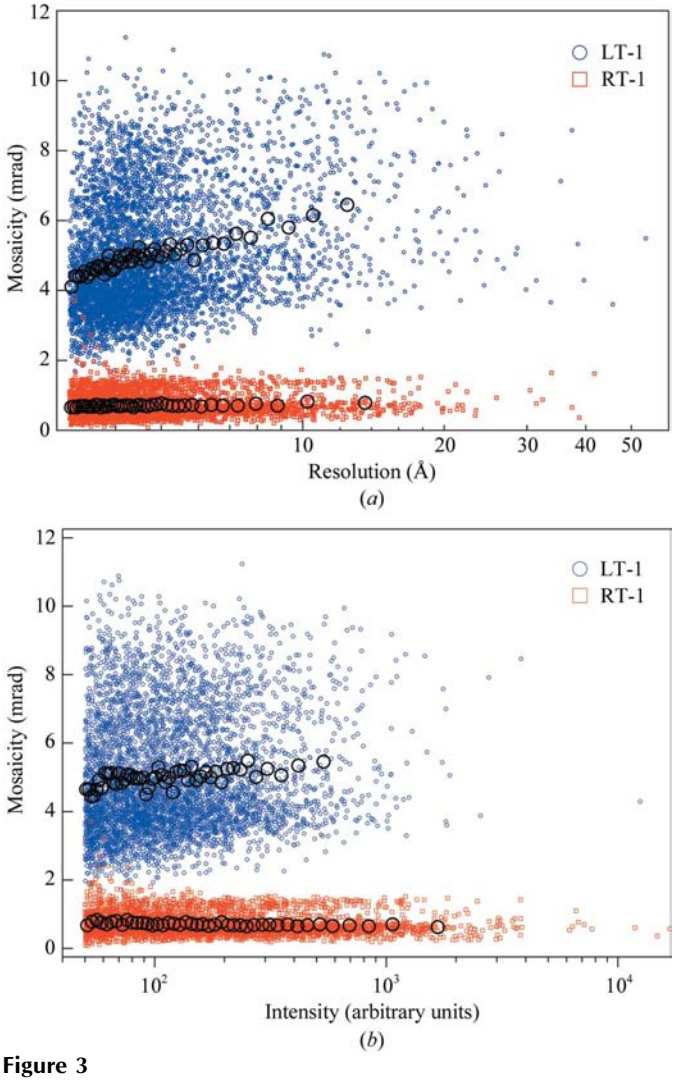

Figure 3
Plots showing the dependence of the mosaicity, η, on (*a*) the resolution, d, and (*b*) the intensity, I. The data are from crystal 10. Red circles are for the first RT cycle (RT-1) and blue circles are the first LT cycle (LT-1). Black circles show averages with bin sizes of 100 reflections.

In the mosaic model of crystal imperfection (Darwin, 1922), the crystal is thought of as an assemblage of groups of unit cells termed mosaic domains. (1) is derived assuming an angular distribution, η, of perfect mosaic domains, which turns infinitesimal reciprocal-lattice points into spherical caps, thus increasing the rocking width. However, the spherical cap may equivalently be replaced with a spherical reciprocal-lattice volume element of finite diameter $2\varepsilon = \eta d^* \cos\theta_{hkl}$ and have the same effect on the rocking width (Greenhough & Helliwell, 1982*a*,*b*). In the data analyzed here, $\cos\theta_{hkl} > 0.98$, so it is a good approximation that $\eta = d^*/2\varepsilon$, which is the angle subtended by the diameter 2ε at the origin of reciprocal space. Here, we interpret η as the angle subtended by a finite-sized reciprocal-lattice volume element and refer to it as the mosaicity.

Adopting the nomenclature of Nave (1998), the angle subtended by the reciprocal-lattice element has three contributions from the domain model. These are the finite domain size (s), the variation in cell dimensions ($\delta a/a$) and the angular distribution of domains (ω). $\delta a/a$ is commonly referred to as strain, while the term mosaicity usually means ω, although here we use mosaicity to mean η. In the simple case that the crystal is broken into domains of equal size, these quantities are related by

$$\eta = \frac{d}{s} + \omega + \frac{\delta a}{a}, \tag{3}$$

which is illustrated in Fig. 4.

The finite domain size, s, increases the width of all reciprocal-space volume elements by the same amount and thus its contribution to η is linear with d. In contrast, both the unit-cell spread and domain-orientation spread increase the reciprocal-space volume width by an amount proportional to $1/d$ and so contribute the same amount to η for all values of d (Nave, 1998; Greenhough & Helliwell, 1982*a*). This can be used to separate the domain-size contribution to η from the other two effects by plotting η *versus* d. The slope of a line fit to this plot gives an estimate of $1/s$, while the y intercept estimates $\omega + \delta a/a$ (Fig. 1, equation 3). Because η *versus* d almost always has a slope greater than or equal to zero, the y intercept is less than the average value of η, so η_{ave} gives an upper limit on ω and $\delta a/a$. Additionally, solving (3) for

$$\frac{d}{\eta} = 1 - \frac{\omega + \delta a/a}{\eta} \tag{4}$$

gives an estimate the fraction of the mosaicity arising from the finite domain size.

Fig. 5 shows an example of our analysis. Data were collected from crystal 10 under three conditions: room temperature (RT-1), low temperature (LT-1) and room temperature again (RT-2). In each case, images were integrated to 3.2 Å resolution, yielding 4331, 5087 and 3056 reflections, respectively, that exceeded the intensity cutoff of 50. These were binned by resolution in groups of 100 and then plotted. In the initial state, $\eta_{avg} = 0.7$ mrad and there is no detectable dependence of

η on d. This suggests a rather large domain size (>10 µm) and puts limits on ω at 0.7 mrad and $\delta a/a$ at 0.0007, suggesting a maximum cell-edge variation of <0.1 Å. After cooling, η_{avg} increases to 5 mrad and there is clearly a dependence of η on d (for a linear fit the slope is 240 µrad Å^{-1} and the intercept is 3.8 mrad). This suggests a domain size of about 0.4 µm (20–25 unit cells on a side) and puts limits on ω at 3.8 mrad and $\delta a/a$ at 0.0038, suggesting a cell-edge variation of <1 Å. Applying (4) shows the fraction of the mosaic spread arising from finite domain size varies from 10% to 40% for the reflections observed (10% at the highest resolution, 3.2 Å, and 40% at the lowest resolution, 12.5 Å). After rewarming the crystal recovers to a domain size of ~3 µm with limiting values of ω at 1.2 mrad and a cell-edge variation of <0.2 Å. This analysis cannot allow us to distinguish ω from $\delta a/a$; however, we address this issue qualitatively in the discussion. This basic procedure was carried out for all crystals and the results are shown in Tables 1 and 2. In the next few sections, we summarize some of the results extracted from these tables.

Table 3
Comparison of the effects on the crystal of adding cryoprotectant at room temperature and then cooling the cryoprotected crystal.

The values given in the table were obtained by averaging over the relevant data shown in Table 1: crystals 9 and 17 for RT (no DMSO), crystals 2, 3, 8, 10, 16 and 18 for RT (30% DMSO) and crystals 2, 3, 8, 10 and 16 for LT. RT and LT indicate room temperature and low temperature, respectively. The values in parentheses indicate the standard deviation of the distribution for (2) and (3) and the difference in the values for the two crystals for (1).

	Unit-cell parameters				
Conditions	Volume (Å^3 × 10^{-3})	a (Å)	b (Å)	c (Å)	Mosaicity η (mrad)
RT (no DMSO) (1)	5417	153.9 (0.1)	171.8 (0.1)	204.9 (0.1)	0.7 (0.0)
RT (30% DMSO) (2)	5356	153.4 (0.1)	171.0 (0.1)	204.1 (0.1)	0.7 (0.1)
LT (30% DMSO) (3)	5064	149.9 (0.4)	168.1 (0.4)	201.0 (0.2)	4.5 (0.4)
Change (1) to (2) (%)	−1.1	−0.3	−0.5	−0.3	0
Change (2) to (3) (%)	−5.4	−2.3	−1.7	−1.5	640

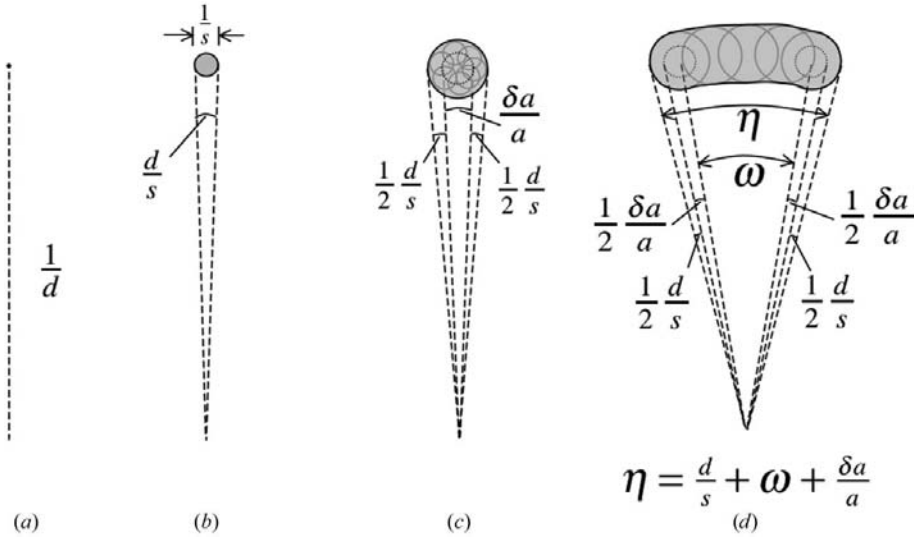

Figure 4
Illustration of the various contributions to η. Each panel shows a hypothetical reciprocal-lattice volume element at the top, with the origin of reciprocal space at the bottom. (*a*) For a perfect infinite crystal, the reciprocal-lattice volume element is a dimensionless point. (*b*) For a perfect finite crystal composed of a single domain the lattice point turns into a sphere, which subtends an angle of d/s. (*c*) For several such domains with a spread of cell dimensions, δa, the sphere becomes larger, subtending an angle of $(d/s) + (\delta a/a)$. (*d*) If the domains are now allowed to be at various orientations with spread ω, the spheres are distributed along an arc of ω. The reciprocal-lattice volume element now subtends an angle of $\eta = (d/s) + \omega + (\delta a/a)$.

3.1. Crystal perfection in the initial state at room temperature

For the two crystals measured at RT without the addition of cryoprotectant, the mosaicity is virtually independent of resolution, while its average value, η_{ave}, is 0.04° or 0.7 mrad (Fig. 6, Table 3). This suggests that $\omega < 0.7$ mrad, $\delta a/a < 7 \times 10^{-4}$ and suggests a domain size, s, greater than 10 µm. That $\delta a/a < 7 \times 10^{-4}$ implies a variation in the cell edges of less than 0.10–0.15 Å, which is similar to the differences between the two crystals, which are about 0.1 Å for the a, b and c cell edges (Table 3).

3.2. Change in the crystal with cryosolution equilibration

Equilibration with the cryosolution causes the RT unit-cell volume to shrink by about 1%, with each individual cell edge decreasing by 0.3–0.5% (Table 3). This is also illustrated in Fig. 7, where the noncryoprotected cell edges and cell volumes are plotted as a reference line. The RT mosaicity, on the other hand, shows no significant change and is still relatively independent of resolution. Thus, at this level of analysis, equilibration with the cryosolution shrinks the unit cell but does not affect the perfection of the crystal.

3.3. Change in the crystal with cooling

After being measured at RT, five crystals with cryoprotectant were expelled from their capillaries, flash-cooled and measured at LT. Cryocooling causes the unit-cell volume to shrink by an additional 5%, with each individual cell edge shrinking by about 2% (Table 3). The mosaicity shows a more dramatic change, increasing about sixfold to η_{avg} = 4.5 mrad (Fig. 6, Table 3) and now has a resolution dependence, yielding ⟨slope⟩ = 210 µrad Å^{-1} and ⟨intercept⟩ = 3.4 mrad. This

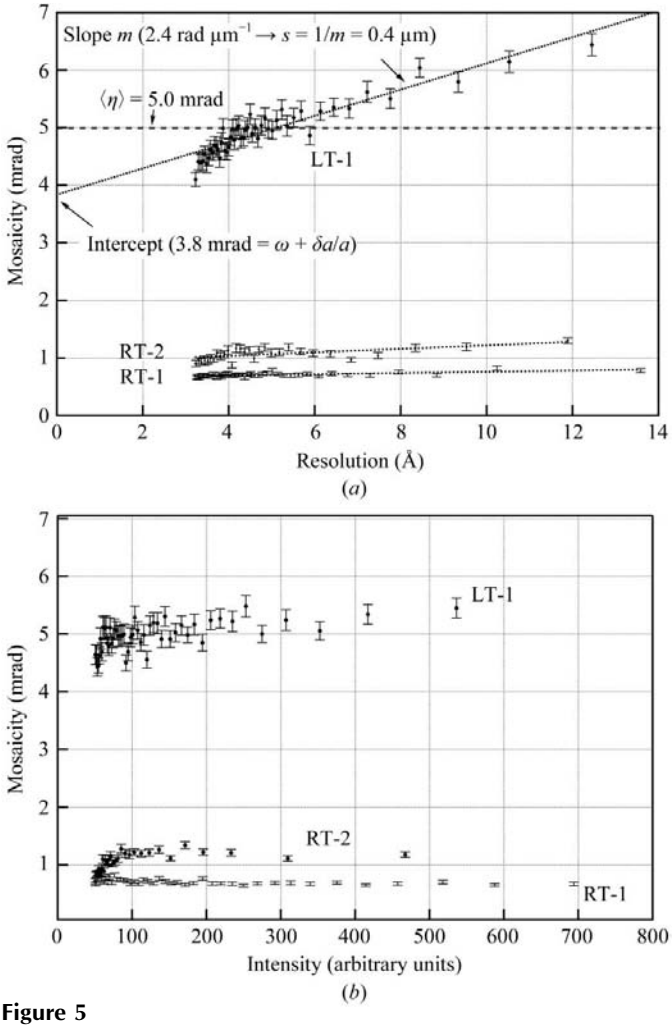

Figure 5
(*a*) Plot showing the dependence of η on the resolution d using binned data (see §2 for details) for the first three passes with crystal 10. The error bars represent the uncertainty of the mean, σ_m, which is the uncertainty of the sample, σ_n, divided by the square root of n: $\sigma_m = \sigma_n/n^{1/2}$. Here, n represents the number of reflections per bin (100). (*b*) Similar plot but for η *versus* I.

increases the limiting values of ω to 3.4 mrad and $\delta a/a$ to 3.4×10^{-3}, which corresponds to a variation in the cell edges of less than 0.5–0.7 Å. By comparison, the actual variation in the a, b and c cell edges between these five LT-1 crystals is 0.4, 0.4 and 0.2 Å, respectively (Table 3). The domain size decreases to the range of 0.5 μm. However, there is variability in the domain size and in some cases the cryocooled crystals appear to have domain sizes of a few micrometres. The finite size of the domains now contributes up to 45% of the mosaicity of the reflections observed.

3.4. Recovery of the crystal with rewarming

Upon rewarming, the crystal cell dimensions recover completely to their original RT values (Fig. 7, Table 4). The mosaicity recovers substantially from 4.5 mrad to about 1.2 mrad, but this is about 70% higher than the original RT value of 0.7 mrad. The recovery of the domain size is also substantial (to a few micrometres), but is incomplete. The domain size now contributes 0–32% of the total mosaicity.

Table 4
The effect on the crystal of successively cooling and returning to room temperature.

All values are for crystals at room temperature (RT) in the presence of DMSO and are average values obtained from Table 1. Cycle 1, crystals 2, 3, 8, 10, 16 and 18; cycle 2, crystals 2, 3, 8, 10 and 16; cycle 3, crystals 3, 8 and 16. Standard deviations are given in parentheses.

	Unit-cell parameters				
Conditions	Volume (Å^3 × 10^{-3})	a (Å)	b (Å)	c (Å)	Mosaicity η (mrad)
DMSO/RT cycle 1 (1)	5356	153.4	171.0	204.1	0.7 (0.1)
DMSO/RT cycle 2 (2)	5364	153.5	171.2	204.2	1.2 (0.2)
DMSO/RT cycle 3 (3)	5359	153.4	171.1	204.3	1.6 (0.1)
Change (1) to (2) (%)	0.2	0.0	0.1	0.1	70
Change (2) to (3) (%)	−0.1	−0.1	−0.1	0.0	30

With the second rewarming cycle, the mosaicity recovers from about 3.6 mrad to 1.6 mrad, while the domain size recovers to a few micrometres. The cell dimensions again recover to their original RT values.

3.5. Hysteresis with multiple RT/LT cycles

As mentioned above, the crystals show increasing disorder (*i.e.* increasing mosaicity) at RT with multiple RT/LT cycles. Overall, the disorder at LT also increases with multiple cycles, although it occasionally decreases over two successive cycles (Fig. 6).

While the crystal order shows hysteresis at both RT and LT, the unit-cell parameters only show hysteresis at LT. In contrast to the RT case, in which the unit-cell parameters are essentially constant from cycle to cycle, at LT the a edge and to a lesser extent the c edge increase in length with successive cooling cycles, while the b edge decreases in length (Fig. 7*b*). In one case (crystal 6) the unit-cell volume increased with each cycle, but this trend was not observed with the other crystals.

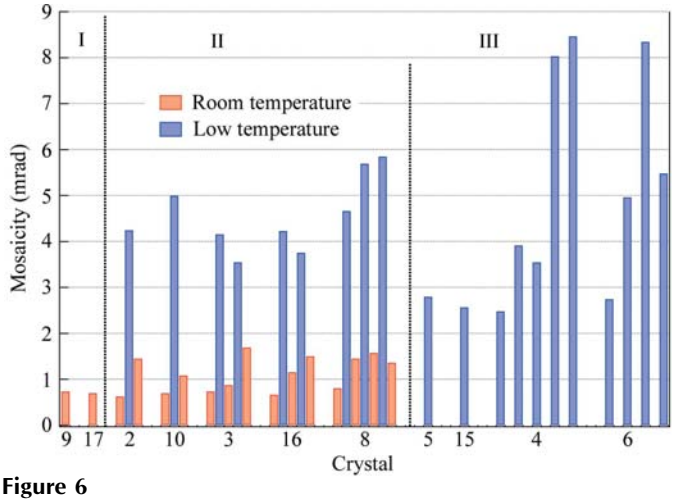

Figure 6
Plot showing the progression of the mosaicity during RT/LT cycling. Room temperature is shown in red and low temperature in blue. Type I experiments are room temperature noncryoprotected. Type II experiments are crystals cycled between RT and LT with diffraction measurements at both temperatures. Type III experiments are the same as type II but diffraction measurements were only made at LT.

3.6. Mosaicity anisotropy

The anisotropy of the mosaicity is illustrated in Fig. 8. In about half of the measurements the ratio of the greatest mosaicity discrepancy between any two of the three reciprocal-lattice directions is >1.5. The figure shows a bias for greater mosaicity in the *b* direction at LT, which is accentuated in later cycles (Table 2). There also does not appear to be a correlation between the RT anisotropy and the LT anisotropy.

3.7. Variability

The crystal parameters at LT have more variability than at RT (Fig. 7*b*). For the type II experiments, the spread of the unit-cell dimensions is on average five times greater at LT than at RT. The spread of the mosaicity is about four times greater at LT than at RT.

4. Discussion

4.1. Crystal perfection at room temperature

The average mosaicity, $\langle\eta_{\rm avg}\rangle$, of RT β-galactosidase crystals is 0.72 mrad. This compares with values of 0.17 mrad for crystals of superoxide dismutase (Bellamy *et al.*, 2000), 0.54 mrad for insulin crystals grown on earth and 0.09 mrad for insulin crystals grown in space (Vahedi-Faridi *et al.*, 2003), all of which were measured using the same methodology as used here.

The value of $\eta_{\rm avg}$ and the dependence of η on resolution, d, suggest limiting values for RT crystal-perfection order parameters: $\omega < 0.7$ mrad, $\delta a/a < 7.2 \times 10^{-4}$ and $s > 10$ µm, which are similar to values reported by Nave for RT lysozyme crystals ($\delta a/a < 3 \times 10^{-4}$ and $s > 0.5$ µm). The domains thus appear to be at least a few hundred unit cells per side. Given that the β-galactosidase crystals are 200–700 µm on each side, at RT these crystals appear to be composed of no more than a few thousand mosaic domains, although possibly far fewer. Any effect on the crystal order by equilibration of these crystals with the DMSO-based cryosolution is undetectable by our current experiment.

4.2. Increase in disorder with cooling

Cryocooling increases $\eta_{\rm avg}$ to about 4.5 mrad. This compares with values of 4.3 mrad for cryocooled insulin crystals (Vahedi-Faridi *et al.*, 2003) and 4.0–4.4 mrad for cryocooled glycerol kinase crystals (Vahedi-Faridi *et al.*, 2005). The sixfold increase in $\eta_{\rm avg}$ of β-galactosidase crystals is

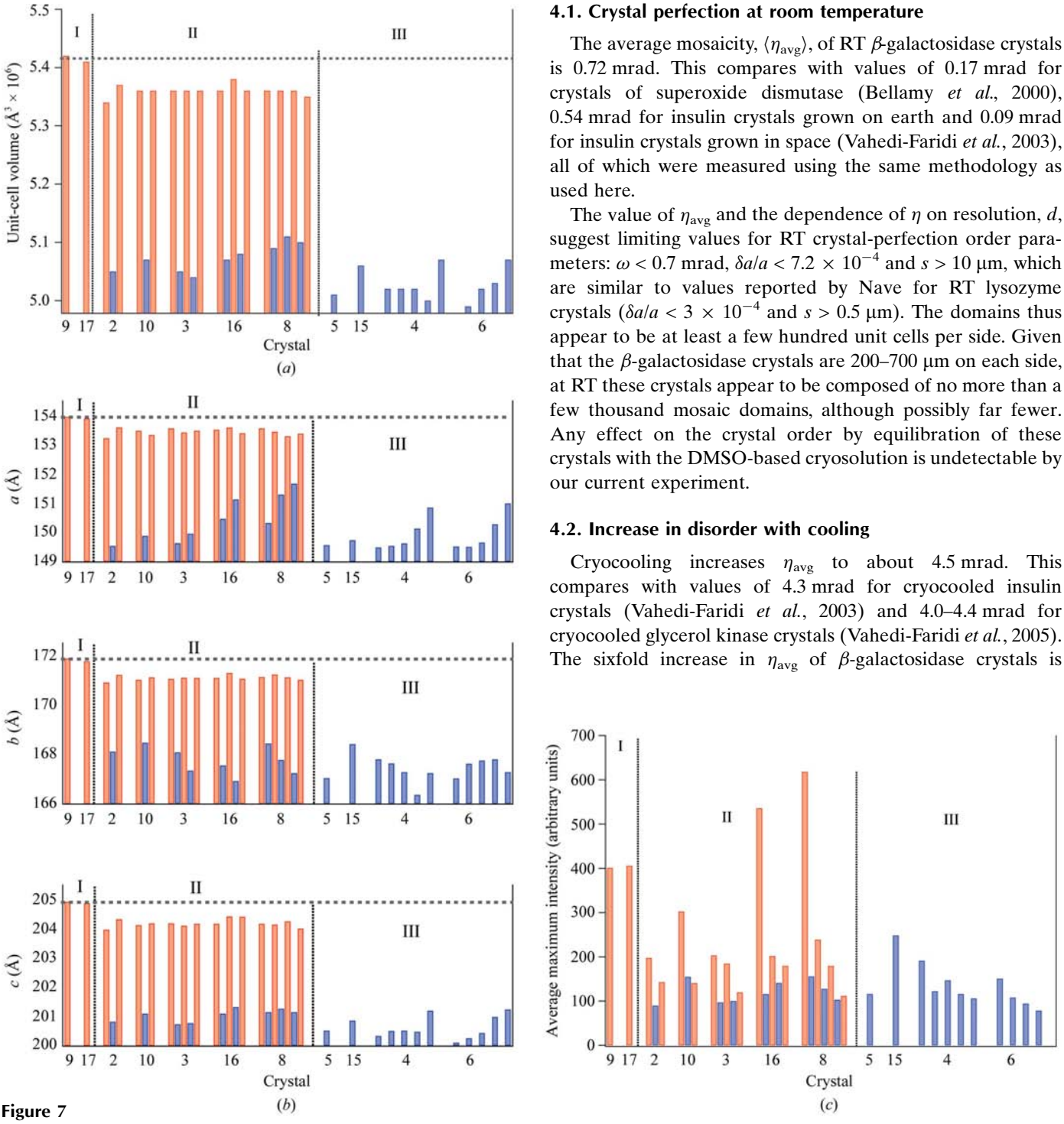

Figure 7
Plot showing the progression of crystal parameters during RT/LT cycling, with room temperature in red and low temperature in blue. (*a*) Unit-cell volume. (*b*) Unit-cell edges. (*c*) Average intensity.

comparable with the eightfold mosaicity increase on cryocooling insulin crystals.

Cryocooling changes the order parameters to $\omega < 3.4$ mrad, $\delta a/a < 3.4 \times 10^{-3}$ and $s \simeq 0.5$ µm, which are similar to the 100 K lysozyme values of $\delta a/a = 5$–15×10^{-3} and $s > 0.5$ µm (Nave, 1998). In the absence of penetrating cryoprotectants even larger mosaicity increases have been observed (Kriminski *et al.*, 2002).

Our interpretation of the dependence of η on d as being caused by a small domain size is dependent on the absence of any systematic errors. For example, weaker data are more likely to be excluded from the analysis by the intensity cutoff. If these data are both higher resolution and higher mosaicity, then excluding them would increase the slope of η *versus* d, causing us to underestimate the domain size s.

With a perfect mosaic domain in an inorganic crystal, a higher intensity reflection does not penetrate as many layers into the domain and is thus broadened because it is produced by fewer unit cells. Thus, with an inorganic crystal a dependence of mosaicity on intensity is expected. However, a protein crystal scatters X-rays more weakly, so that even strong reflections are scattered by all unit cells in a domain (Helliwell, 1992). Thus, a dependence of mosaicity on intensity is not expected for a protein crystal in general.

In most of the cases presented here the mosaicity is only very weakly correlated with intensity (for example, Fig. 5*b*, RT-1). In some cases (2 LT-1, 4 LT-4, 4 LT-5, 6 LT-2, 6 LT-3, 6 LT-4, 8 LT-3, 10 LT-1, 10 RT-2, 12 RT-2, 8 RT-4), there is a strong direct correlation between mosaicity and intensity that is somewhat weaker than the correlation between mosaicity and d-spacing (for example, compare the LT-1 plots in Figs. 5*a* and 5*b*). In these cases, we can explain the intensity dependence as an effect of the resolution dependence, since higher intensity reflections typically have lower d-spacings and thus larger mosaicities in the cases of small domain sizes.

Occasionally (8 RT-2, 10 RT-2, 16 RT-2, 4 LT-2), the mosaicity is relatively independent of intensity over most of the range, but then drops quickly between $I = 100$ and $I = 50$ (for an example, see Fig. 5*b*, RT-2). This raises some concern over the value of our intensity cutoff, which was used to prevent excessive integration of noise and was chosen to give a normal mosaicity distribution, but could have been chosen too low for these few crystals. As a check, we repeated the complete analysis with all crystals using intensity cutoffs of $I_{\rm min} = 100$ and also $I_{\rm min} = 30$ and found that the overall result was robust to these cutoffs. The slope of η *versus* d was about the same for all cutoffs, but more importantly its behavior with RT/LT cycling was the same. That is, it increased with cooling and decreased again with rewarming (see below). In summary, the slopes of η *versus* d do not appear to be artifacts arising from the somewhat arbitrary nature of the intensity cutoff or from the natural difficulty of accurately measuring weak data.

The mosaicity increase with cooling thus appears to partly be a consequence of a decrease in domain size. A domain-size decrease from >10 µm to ∼0.5 µm corresponds to a decrease from >500–700 unit cells per side to 25–35 unit cells per side. Similarly, Lovelace *et al.* (2006) performed fine φ-slicing in concert with topography measurements using a CCD camera with 8 µm resolution on a lysozyme crystal. They made measurements at both RT and LT on the same reflections of the same crystal and observed a decrease in domain size and an increase in domain number with cryocooling. In the β-galactosidase case reported here, the data suggest that domain-size effects account for between 0 and 45% of the observed mosaicity increase in cooling crystals of β-galactosidase, depending on the crystal and the resolution of any particular reflection. The remainder of the mosaicity increase arises from either an increase in the cell-dimension spread, $\delta a/a$, or the angular separation of domains, ω.

As mentioned above, the effect of an increased ω is to turn reciprocal-lattice points into spherical caps. During data collection, these caps are projected onto the detector, appearing as arcs centered on the direct beam (Fig. 9*a*). In extreme cases, the diffraction pattern starts to look like a powder pattern (Fig. 9*b*). Observing such arcs indicates that the angular spread between domains is dominating over the cell-dimension spread. We see clear indications of this behavior in a few crystals, two patterns from which are shown in Fig. 9. The clearest cases of this are with later cycles of crystals 4 and 6, suggesting that one way hysteresis builds up is in the angular spread between domains. However, in most cases ω does not dominate, suggesting that $\delta a/a$ plays a significant role in nearly all of our samples. There are also clear indications of anisotropy in the mosaicity from the diffraction patterns, so that for some directions $\delta a/a$ could be the major effect while in other directions ω could dominate. This is discussed further below.

In a fine φ-slicing experiment comparing earth-grown with microgravity-grown

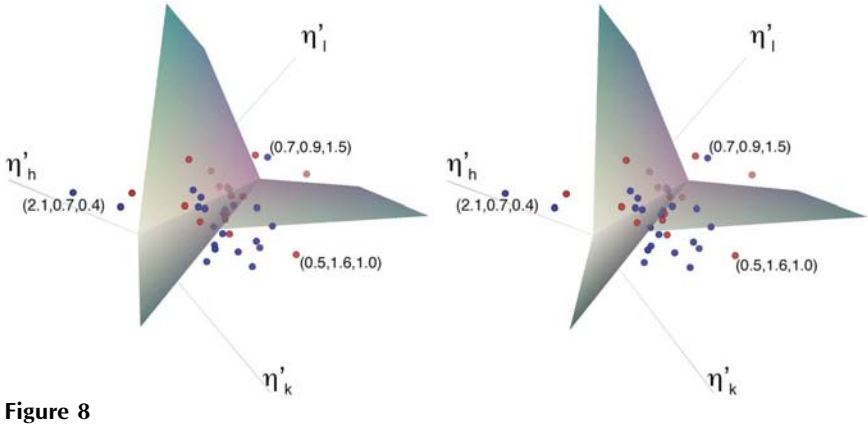

Figure 8
Wall-eyed stereo image showing normalized mosaicity anisotropy, in which each point represents one crystal under one condition, plotted according to $(\eta'_h, \eta'_k, \eta'_l) = (\eta_h/\eta, \eta_k/\eta, \eta_l/\eta)$. The values of these coordinates are given for three of the plotted points for reference. The data occupy three sectors, depending on which direction has the largest mosaicity. The distance from the center line gives a qualitative measure of the degree of anisotropy. As such, both RT and LT have about the same degree of anisotropy. Additionally, the LT anisotropy is biased in the b direction, while at RT there is no clear anisotropy bias.

insulin crystals, cryocooling caused the reflection profiles to show multiple peaks that could be fitted by multiple Gaussians (Vahedi-Faridi *et al.*, 2003). Some of the profiles in Fig. 2 also show multiple peaks. These peaks may represent an intermediate level of organization within the crystals, in which there are groups of mosaic domains oriented significantly differently from other groups of mosaic domains. The angular separation of these groups of domains would produce the separation of the centers of the peaks, while within each group there would be multiple mosaic domains with angular and cell-dimension spreads and finite sizes that give each peak in the profile its width.

The search for the appropriate cooling conditions for the β-galactosidase crystals started with brief passes (1–4 s) of the crystal through solutions of glycerol, PEG 400, ethylene glycol, PEG 500 monomethyl ether, 2-methyl-2,4-pentanediol, glucose, sucrose and DMSO. This technique suggested that the most promising cryoprotectant was DMSO. Further investigations with DMSO showed that a slow equilibration to about 30%(*v*/*v*) cryoprotectant was optimal, with both higher and lower cryoprotectant producing more diffuse scatter, a higher mosaicity and a lower resolution limit. Similarly, PEG 400 can serve as an effective cryoprotectant with an optimum of about 40%.

The fact that the mosaicity still increases sixfold under apparently the best conditions that could be found suggests that the flash-cooling process is still far from perfect. Further work needs to be performed in order to understand the discrepancy between the RT order and the LT order under what seem to be optimal cooling conditions.

4.3. Mosaicity recovery with rewarming

About 75% of the sixfold increase in the mosaicity that occurs on flash-cooling is recoverable with rewarming (Fig. 6). This apparent reversibility is consistent with previous results using a home source (Juers & Matthews, 2001), but is more clearly demonstrated here. The reversibility of flash-cooling has been studied explicitly (Harp *et al.*, 1998; Samygina *et al.*, 2000) and also implicitly in the many examples of cryo-annealing. However, this study is the first detailed report of reversibility in flash-cooling that looks at crystal order in both temperature states.

Because the slope of η *versus* d decreases with rewarming, it suggests that the domain sizes recover somewhat towards their initial RT values of >10 µm. This suggests an inherent reversibility in the cooling-induced damage process that leads to domain recovery with warming. Kriminski *et al.* (2002) observed a domain-size increase from less than a few micrometres to about 20 µm in lysozyme crystals when using a somewhat different annealing procedure in which the crystal was warmed to 240 K rather than RT. They suggested that lattice stresses cooled into the crystal are released upon warming, allowing domain growth at the higher temperature. Our observations are consistent with this idea and furthermore point to the potential benefit of a protocol in which cooling is carried out slowly, preventing such stresses from being introduced in the first place. However, the problem with slow cooling is that ice crystals may result if vitrification of the cryosolvent is not successful.

Our data also suggest not only a recovery of domain size but also either a realignment of domains with each other or a

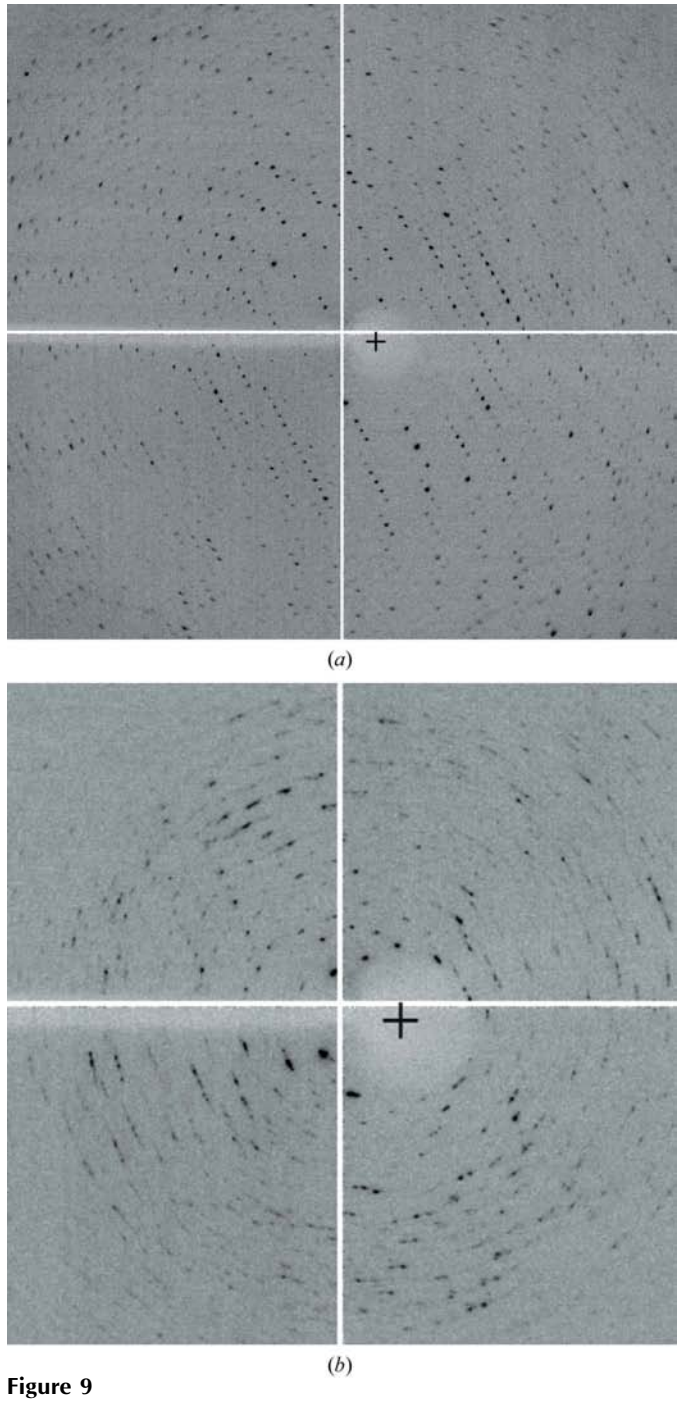

Figure 9
Diffraction images illustrating two cases in which the angular spread between domains, ω, is clearly a significant effect. (*a*) Crystal 6 LT-4. Spots some distance from the center are all small arcs mostly centered at the beam center (indicated by the cross). The arc length increases the further from the beam center, as expected. The corners are 4.2–4.4 Å. (*b*) Crystal 5 LT-2. A more extreme case, showing how the diffraction pattern starts to look like a powder pattern if ω is very large. In this case, ω was too large to accurately index the crystal, so this exposure does not appear in the tables or other figures.

recovery from the strain reflected in unit-cell variation. Kriminski and coworkers mainly observed the release of strain in the form of $\delta a/a$, but maintenance of the relative orientation of domains. This could be because the 240 K annealing temperature used in Kriminski *et al.* (2002) is too low to permit global realignment of domains, whereas this would be reasonable with RT annealing.

4.4. Hysteresis of crystal parameters with flash-cooling

Fig. 6 shows that although the increase in mosaicity with flash-cooling is largely recoverable, there is a certain amount of hysteresis. The RT mosaicity increases by about 0.6 mrad per cycle. Overall, the RT spot profiles for the initial state are smooth and can usually be well fitted with a single Gaussian. The RT profiles for successive cycles are wider and somewhat less smooth (Fig. 2). In some cases the profiles appear to be composed of multiple Gaussians. Because the crystal orientation was lost with remounting, it was not possible to perform a rigorous analysis by (for example) following the same location in reciprocal space through all RT/LT cycles. Nevertheless, the results show that there is measurable damage to the crystal at both RT and LT as the experiments progress. Two possible sources of this hysteresis are irreversible damage from the cool–thaw process, including damage from manipulating the crystals, and irreversible damage from ionizing radiation. Our data suggest that both processes may occur but that radiation damage has the greater effect.

4.4.1. Changes from radiation exposure. For evidence of the impact of radiation damage at RT, consider first that η tends to be larger and s tends to be smaller with the first cooling cycle if the crystal was first measured at RT (Table 2). This suggests that radiation damage at RT is exacerbating damage caused by cooling, perhaps by loosening up intermolecular contacts, allowing easier breakage into smaller domains, or *via* the formation of gases within the crystal (Southworth-Davies & Garman, 2007).

Similarly, radiation exposure at RT appears to increase the unit-cell volume at LT when compared with crystals not exposed at RT (type III crystals; Fig. 7*a*). In this context, a number of studies performed in the cryogenic state only have shown that radiation exposure produces an increase in the LT unit-cell volume (Ravelli *et al.*, 2002; Müller *et al.*, 2002; Murray & Garman, 2002). One possible explanation for this is a build-up of electrostatic repulsion during the exposure (Ravelli *et al.*, 2002). Here, the experimental conditions are quite different since the crystals are cycled between LT and RT, but nevertheless an increase in the LT unit-cell volume was seen, which in this case appears to be a consequence of radiation exposure at RT. The build-up of electrostatic charge would seem to be impossible here, since the crystal clearly has ample opportunity to dissipate any electrostatic charge between LT exposures. Two other possibilities include damage during the RT exposure to residues normally involved in LT crystal contacts, which in this case are quite different from RT crystal contacts (Juers & Matthews, 2001), or an alteration of bulk-solvent thermal expansion properties from the radiation (Juers & Matthews, 2004).

Radiation damage from LT exposure also appears to be in effect. Type III crystals were only exposed to X-rays at LT and were organized into two groups: type IIIa crystals had data collected after each cooling phase and type IIIb crystals had data collected after the second cooling phase. Type IIIa crystals showed $\langle\eta_{\rm avg}\rangle$ = 2.7 mrad after the first cooling phase, which increased to 4.4 mrad after the second cooling phase, while type IIIb crystals showed $\langle\eta_{\rm avg}\rangle$ = 2.9 mrad after the second cooling phase. Thus, the exposure of type IIIa crystals after the first cooling phase appears to increase the mosaicity after the second cooling phase relative to the type IIIb crystals, which were not exposed after the first cooling phase. This is likely to be a consequence of the mobilization of free radicals created during the first exposure at 100 K during the warming phase.

Although we did not quantify the dosage, after accounting for the attenuation by aluminium this radiation exposure corresponds to about a total of 75 s in the full-strength beam, which is not unusual when screening crystals. There is thus a conundrum for annealing *via* RT/LT cycling in which the radiation exposure used to monitor LT crystal quality can produce the damage it is intended to assess. It therefore would appear advantageous to (i) use fewer shorter exposures to limit free-radical buildup during frames used to assess diffraction and (ii) use a shorter warming phase with annealing to limit the damage from mobilized free radicals. The development of non-X-ray methods to assess crystal order at LT would also be beneficial.

4.4.2. Hysteresis from cool–thaw processes. The small difference between the value of $\langle\eta_{\rm avg}\rangle$ for type IIIa and type IIIb upon first X-ray exposure (2.7 mrad after the first cooling phase *versus* 2.9 mrad after the second cooling phase) could reflect damage from cool–thaw processes alone. However, this difference is insignificant given the uncertainties in the mosaicity measurements (Table 2), which suggests that hysteresis from cool–thaw processes, if it exists, appears to be smaller than the hysteresis from radiation-damage effects. Consider also control crystal 12, which was only exposed at LT prior to the second RT cycle. This crystal would not be subject to RT damage processes, yet shows parameters typical of an RT-2 (that is, RT/LT/RT) crystal. This points to damage from cool–thaw processes and/or radiation damage from the mobilization of free radicals produced during the LT exposure. In this case, these two possibilities cannot be distinguished.

4.5. Variability of crystal parameters: the competition between the stochastic nature of cryocooling and the inevitable radiation and cool–thaw-induced degradation

All crystal parameters (unit-cell dimensions and order parameters) show greater variability at LT than at RT. This variability appears to occasionally win over the hysteresis, resulting in a crystal with reduced LT disorder by using RT/LT cycling.

The greater variability of the crystal parameters at LT suggests that there are aspects of the flash-cooling procedure that are poorly controlled. The variation is seen from crystal to crystal and in repeated experiments with the same crystal. Some possible sources of this variability include the amount of mother liquor surrounding the crystal, the orientation of the crystal in the cryoloop, the orientation of the crystal in the cryostream, the amount of time taken to transfer the crystal to the cryostream, the degree of manipulation of the crystal in its drop and the crystal size. The crystals will also suffer a varying amount of mechanical stress upon mounting, dismounting and transfer through cryosolutions. To avoid variation, we attempted to uniformly blot the crystals to minimize the amount of mother liquor surrounding the crystal during cooling and to transfer the crystals in a uniform amount of time. The issue of crystal size is addressed below. However, all of these factors are difficult to control.

In a few cases, the low-temperature mosaicity decreased by 10–30% between two successive RT/LT cycles. Other researchers have reported similar or somewhat larger improvements (Harp *et al.*, 1998; Vahedi-Faridi *et al.*, 2005). In our case, this improvement appears to be the result of the inherent stochastic nature of the cooling procedure combined with the somewhat surprising resilience of the crystals to damage by cooling.

4.6. Anisotropy in the mosaicity and the crystal dimensions

The crystals show a range of mosaicity anisotropy both at RT and LT (Fig. 8). The mosaicity will not in general have a higher symmetry than the space group, so the anisotropy in the room-temperature mosaicity is not surprising for an orthorhombic unit cell. The mosaicity anisotropy at LT is also not surprising and is easily visible in the diffraction patterns.

We looked for correlations between the crystal dimensions and the mosaicity or mosaicity anisotropy. The mosaicity was not well correlated with either the crystal volume, which ranged an order of magnitude from about 0.02 mm^3 to about 0.3 mm^3, or with the crystal habit, which ranged from relatively uniform pyramids to slabs 2.5 times as long as they were thick (data not shown). One might expect to find smaller crystals to have lower mosaicities and we did find small mosaicities with some small crystals, but other small crystals had larger mosaicities.

The mosaicity anisotropy was weakly correlated with some crystal parameters (data not shown). Larger crystals were generally more isotropic than smaller crystals. Crystals that were isotropic in shape were generally more isotropic in mosaicity than anisotropically shaped crystals. However, these correlations were weak and further experiments would need to be performed in order to verify them.

As mentioned above, crystals at LT had greater mosaicity along the *b* direction (Fig. 8), while at RT there did not seem to be a preference for the direction of maximum mosaicity. The type III crystals 4 and 6, which went through multiple RT/LT cycles but for which diffraction data were collected only at LT, showed a clear preference (eight of nine measurements) for maximum mosaicity in the *b* direction. Type II crystals were equally likely to have η_h and η_k maximum at LT, but showed no clear preference at RT. Furthermore, type II crystals had a 2/3 probability of switching the direction of maximum η either when cooling or when thawing, which is what would be expected from chance alone.

In summary, there appears to be no correlation between the mosaicity anisotropies at LT and at RT. In other words, the direction of the greatest disorder at LT is independent of the state of the crystal at RT (and *vice versa*). This suggests that the anisotropy is determined by the cooling (or thawing) process itself. Since at LT the disorder is greatest parallel to the *b* axis, there may be something about the crystal packing that tends to cause the cooling-induced stress to be relieved along lattice contacts and to create more domain boundaries perpendicular to *b* and consequently a smaller domain size along *b*. Alternatively, there may be something about the packing that causes greater strain ($\delta a/a$) to build up in the *b* direction, for example by directing stress from solvent expansion or contraction in this direction. Furthermore, the later cycles favor the LT anisotropy in the *b* direction, as well as a decrease in the lengths of the LT *b* cell edge. There thus appears to be a correlation between the anisotropy in the *b* direction and the decrease of the length of the cell edge in this same direction. Whatever the cause of the LT mosaicity anisotropy, the RT anisotropy appears to be unrelated to, or at least overwhelmed by, this mechanism.

5. Summary and conclusion

We have used a fine φ-slicing technique in combination with a CCD detector and a highly collimated X-ray beam to determine the mosaicity of a statistically significant number of reflections for each of several crystals of *E. coli* β-galactosidase repeatedly cycled between RT and LT. These measurements indicate that cryogenic cooling increases crystal disorder by decreasing the size of mosaic domains and increasing the relative spread in domain orientation and/or the spread in cell dimensions within the crystal. Furthermore, with this particular system rewarming the crystal causes substantial recovery of the crystal order, including the increase in domain size. However, the recovery is incomplete, mainly owing to radiation-damage effects. The large degree of recovery combined with the apparent stochastic nature of the cooling phase suggests that repeated RT/LT cycling may yield improved LT crystal order. The recovery opens the possibility of improved LT order, while the stochasticity provides a mechanism of achieving it. However, the incomplete nature of the recovery suggests that only a few RT/LT cycles should be undertaken in order to minimize the build-up of crystal damage.

We suggest that the conclusions derived from our results are of general applicability for many protein crystals, especially those for which annealing can be successfully performed. Crystals of *E. coli* pyrophosphatase, which diffract to better than 1.2 Å, were subjected to ten rounds of RT/LT cycling on beamline X11 at DESY (Deutsches Elektronen-Synchrotron)

with improved LT diffraction throughout (Samygina *et al.*, 2000). In an experiment in which a β-galactosidase crystal was subjected to 29 rounds of RT/LT cycling under ambient humidity conditions (D. H. Juers & B. W. Matthews, unpublished observations), the mosaicity initially decreased and the signal-to-noise at 2.8 Å increased to about 5.0. At cycle 13 the mosaicity abruptly increased and the signal-to-noise dropped to 3.5. In subsequent cycles the signal-to-noise gradually degraded until at cycle 28 there was essentially no signal at 2.8 Å. On the 29th LT/RT/LT cycle, which was performed under high humidity, the crystal recovered, with a signal-to-noise at 2.8 Å of 2.6. This particular experiment was carried out on a home X-ray source, so radiation damage should be less significant. It also used a somewhat different annealing protocol from the current experiment, normally termed '*in situ*' annealing, in which the crystal is left in place on the cryoloop for a few seconds before recooling. In this particular case the cryoprotectant was probably initially slightly below the optimum concentration. During successive cycles water vapor diffused out of the crystals, at first allowing the cryoprotectant concentration to increase towards its optimum, but then causing the cryoprotectant to become too concentrated. The final 29th cycle under high humidity allowed the cryoprotectant to recover towards its optimal concentration. This experiment and the pyrophosphatase case are two examples in which many more RT/LT cycles are possible than found in the current study. Clearly, further work needs to be performed on a wider variety of systems in order to provide an adequate picture of cooling-induced damage and methods for recovery.

We thank Lisa Keefe and Andy Howard at IMCA-CAT for assistance with data collection and Mike Quillin, Walt Baase and Richard Kingston for helpful discussions. This work was supported in part by NIH grant GM20066 to BWM and by NASA grants NAG8-1580, NAG8-1380 and NAG8-1836. HDB is partially supported by the Louisiana Governor's Biotechnology Initiative. Use of the IMCA-CAT beamline 17-ID at the Advanced Photon Source was supported by the companies of the Industrial Macromolecular Crystallography association through a contract with Illinois Institute of Technology. Use of the Advanced Photon Source was supported by the US Department of Energy, Office of Science, Office of Basic Energy Sciences under Contract No. W-31-109-Eng-38.

References

Bellamy, H. D., Snell, E. H., Lovelace, J., Pokross, M. & Borgstahl, G. E. O. (2000). *Acta Cryst.* D**56**, 986–995.
Borgstahl, G. E. O., Vahedi-Faridi, A., Lovelace, J., Bellamy, H. D. & Snell, E. H. (2001). *Acta Cryst.* D**57**, 1204–1207.
Darwin, C. G. (1922). *Philos. Mag.* **43**, 800–829.
Ellis, M. J., Antonyuk, S. & Hasnain, S. S. (2002). *Acta Cryst.* D**58**, 456–458.
Ferrer, J.-L. & Roth, M. (1998). *J. Appl. Cryst.* **31**, 523–532.
Garman, E. (1999). *Acta Cryst.* D**55**, 1641–1653.
Garman, E. F. & Doublié, S. (2003). *Methods Enzymol.* **368**, 188–216.
Garman, E. F. & Owen, R. L. (2006). *Acta Cryst.* D**62**, 32–47.
Garman, E. F. & Schneider, T. R. (1997). *J. Appl. Cryst.* **30**, 211–237.
Greenhough, T. J. & Helliwell, J. R. (1982*a*). *J. Appl. Cryst.* **15**, 338–351.
Greenhough, T. J. & Helliwell, J. R. (1982*b*). *J. Appl. Cryst.* **15**, 493–508.
Hanson, B. L., Harp, J. M. & Bunick, G. R. (2003). *Methods Enzymol.* **368**, 217–235.
Harp, J. M., Hanson, B. L., Timm, D. E. & Bunick, G. J. (1999). *Acta Cryst.* D**55**, 1329–1334.
Harp, J. M., Timm, D. E. & Bunick, G. J. (1998). *Acta Cryst.* D**54**, 622–628.
Helliwell, J. R. (1992). *Macromolecular Crystallography with Synchrotron Radiation.* Cambridge University Press.
Hope, H. (1988). *Acta Cryst.* B**44**, 22–26.
Juers, D. H., Jacobson, R. H., Wigley, D., Zhang, X.-J., Huber, R. E., Tronrud, D. E. & Matthews, B. W. (2000). *Protein Sci.* **9**, 1685–1699.
Juers, D. H. & Matthews, B. W. (2001). *J. Mol. Biol.* **311**, 851–862.
Juers, D. H. & Matthews, B. W. (2004). *Acta Cryst.* D**60**, 412–421.
Kriminski, S., Caylor, C. L., Nonato, M. C., Finkelstein, K. D. & Thorne, R. E. (2002). *Acta Cryst.* D**58**, 459–471.
Leslie, A. G. W. (1992). *Jnt CCP4/ESF–EACBM Newsl. Protein Crystallogr.* **26**.
Lovelace, J. & Borgstahl, G. E. O. (2003). *J. Appl. Cryst.* **36**, 1101–1102.
Lovelace, J. J., Murphy, C. R., Bellamy, H. D., Brister, K., Pahl, R. & Borgstahl, G. E. O. (2005). *J. Appl. Cryst.* **38**, 512–519.
Lovelace, J. J., Murphy, C. R., Pahl, R., Brister, K. & Borgstahl, G. E. O. (2006). *J. Appl. Cryst.* **39**, 425–432.
Lovelace, J., Snell, E. H., Pokross, M., Arvai, A. S., Nielsen, C., Xuong, N.-H., Bellamy, H. D. & Borgstahl, G. E. O. (2000). *J. Appl. Cryst.* **33**, 1187–1188.
Lovelace, J. J., Soares, A. S., Bellamy, H. D., Sweet, R. M., Snell, E. H. & Borgstahl, G. E. O. (2004). *J. Appl. Cryst.* **37**, 481–485.
Mitchell, E. P. & Garman, E. F. (1994). *J. Appl. Cryst.* **27**, 1070–1074.
Müller, R., Weckert, E., Zellner, J. & Drakopoulos, M. (2002). *J. Synchrotron Rad.* **9**, 368–374.
Murray, J. & Garman, E. (2002). *J. Synchrotron Rad.* **9**, 347–354.
Nave, C. (1998). *Acta Cryst.* D**54**, 848–853.
Parkin, S. & Hope, H. (2003). *Acta Cryst.* D**59**, 2228–2236.
Ravelli, R. B. G., Theveneau, P., McSweeney, S. & Caffrey, M. (2002). *J. Synchrotron Rad.* **9**, 355–360.
Rodgers, D. W. (1994). *Structure*, **2**, 1135–1140.
Samygina, V. R., Antonyuk, S. V., Lamzin, V. S. & Popov, A. N. (2000). *Acta Cryst.* D**56**, 595–603.
Snell, E. H., Judge, R. A., Crawford, L., Forsythe, E. L., Pusey, M. L., Sportiello, M., Todd, P., Bellamy, H., Lovelace, J., Cassanto, J. M. & Borgstahl, G. E. O. (2001). *Cryst. Growth Des.* **1**, 151–158.
Southworth-Davies, R. J. & Garman, E. F. (2007). *J. Synchrotron Rad.* **14**, 73–83.
Vahedi-Faridi, A., Lovelace, J., Bellamy, H. D., Snell, E. H. & Borgstahl, G. E. O. (2003). *Acta Cryst.* D**59**, 2169–2182.
Vahedi-Faridi, A., Stojanoff, V. & Yeh, J. I. (2005). *Acta Cryst.* D**61**, 982–989.
Weik, M., Schreurs, A. M. M., Leiros, H.-K. S., Zaccai, G., Ravelli, R. B. G. & Gros, P. (2005). *J. Synchrotron Rad.* **12**, 310–317.
Wormington, M., Panaccione, C., Matney, K. M. & Bowen, D. K. (1999). *Philos. Trans. R. Soc. London Ser. A*, **357**, 2827–2848.
Yeh, J. I. & Hol, W. G. J. (1998). *Acta Cryst.* D**54**, 479–480.